

Surface chemistry and diffusion of trace and alloying elements during in vacuum thermal deoxidation of stainless steel

Lin Zhu¹  | Ali Al-Sakeeri² | Filip Lenrick^{2,3,4}  | Oskar Darselius Berg^{4,5} | Per Sjödin⁵ | Alexei A. Zakharov¹ | Axel Knutsson⁵ | Anders Mikkelsen^{2,3} 

¹MAX IV Laboratory, Lund University, Lund, Sweden

²Department of Physics, Lund University, Lund, Sweden

³NanoLund, Lund University, Lund, Sweden

⁴Department of Mechanical Engineering, Lund University, Lund, Sweden

⁵Materials Technology & Chemistry, Alfa Laval, Lund, Sweden

Correspondence

Anders Mikkelsen, Department of Physics, Lund University, Lund, Sweden.
Email: anders.mikkelsen@sljus.lu.se

Funding information

Vinnova; Swedish Foundation for Strategic Research; Swedish Research Council

Removal of the native surface oxide from steel is an important initial step during vacuum brazing. Trace and alloying elements in steel, such as Mn, Si, and Ni, can diffuse to the surface and influence the deoxidation process. The detailed surface chemical composition and grain morphology of the common stainless-steel grade 316L is imaged and spectroscopically analyzed at several stages of in-vacuum annealing from room temperature up to 850°C. Measurements are performed using synchrotron-based X-ray photoemission and low-energy electron microscopy (XPEEM/LEEM). The initial native Cr surface oxide is amorphous and unaffected by the underlying Fe grain morphology. After annealing to ~700°C, the grain morphology is seen at the surface, persisting also after the complete oxygen removal at 850°C. The surface concentration of first Mn and then Si increases significantly when annealing to 500°C and 700°C, respectively, while Ni and Cr concentrations do not change. Mn and Si are not located only in grain boundaries or clusters but are distributed across over the surface. Both Mn and Si appear as oxides, while Cr oxide becomes metallic Cr. Annealing from 500°C up to 850°C leads to the removal of first the Mn and then Si oxides from the surface, while Cr and Fe are completely reduced to metals. Deoxidation of Cr occurs faster at the grain boundaries, and the final Cr metal surface content varies between the grains. The findings are summarized in a general qualitative model, relevant for austenite steels.

KEYWORDS

annealing, deoxidation, diffusion, LEEM, microscopy, PEEM, steel alloys, surface, vacuum, XAS, XPS

1 | INTRODUCTION

Stainless steels were introduced at the beginning of the 20th century, and in the ensuing half century, academia and manufacturers developed a large family of stainless steels serving many different applications. The austenitic (face centered cubic, FCC) stainless-steel grade 316L (UNS-S31603/EN-1.4404), studied in this work, is one of the

most common iron-based alloys that is used for a wide range of applications from cookware to industrial equipment. On all stainless steels, a native oxide layer, usually termed “passive layer,” acts as an excellent barrier against corrosion. It is generally accepted that the few nanometers thick protective oxide is a result of oxidation of the Cr (present in the base alloy) at the steel surface.^{1,2} Beyond Cr (16–18% wt.), 316L is also alloyed with Ni (10–14% wt.), Mo (2–3% wt.), and

This is an open access article under the terms of the Creative Commons Attribution License, which permits use, distribution and reproduction in any medium, provided the original work is properly cited.

© 2021 The Authors. *Surface and Interface Analysis* published by John Wiley & Sons Ltd.

Mn (<2% wt.). The primary purpose of Ni and Mn is to stabilize the austenitic structure while Mo increases the resistance to pitting corrosion.² In addition, low levels (<1% wt.) of several other elements are present in the steel such as Si (<1% wt.), P (<0.03% wt.), C (<0.03% wt.), and S (<0.045% wt.), which are trace elements from the mining- and manufacturing process.

Many products manufactured in 316L require metal joining such as welding or brazing operations, which represent a significant global value³ and are still highly active areas of research.⁴ In the widely used high-volume manufacturing process, vacuum brazing, the steel is exposed to elevated temperatures in batch furnaces with a filler metal, usually consisting of copper or nickel alloys. During elevated temperature, the filler metal melts and wets the stainless steel forming a brazed joint. The molten filler metals are considered as high surface energy liquids. Wetting of the solid stainless steel with the molten filler metal is possible only if the interfacial bond between the two is strong, which requires a metallic or chemical character of the bond. Therefore, the presence of an oxide can influence the wetting during the brazing, resulting in a poor quality of the brazed joint, and failure can occur in the end product. Hence, a complete and controlled deoxidation of the native oxide is decisive for successful stainless-steel vacuum brazing operations. While oxidation of stainless steel has been investigated in significant detail, the deoxidation of the native oxide is much less studied.

The temperature-dependent stability of compounds of metals, its oxides, and oxygen can generally be found in the Ellingham diagram.^{5,6} However, considering a modern full-scale industrial vacuum brazing furnace, the O partial pressure level will never be enough to permit reduction of the chromium oxide according to the Ellingham diagram. Instead, there exist several explanations how the initial deoxidation transpires such as difference in thermal expansion⁶ and surface diffusion of carbon.⁷ However, because of the challenges in characterizing a nanometer thin oxide in combination with high temperature, no consensus in this area exists. A detailed understanding of the deoxidation and the role of both the alloying and trace elements are essential for a more efficient and controlled manufacturing, and the development of new metal joining methods and stainless steels optimized for vacuum brazing.

In the last 20 years, X-ray photoelectron spectroscopy and photoemission electron microscopy (XPS and XPEEM) were used in several studies of the surface of stainless steel.^{8–17} XPS was used to reveal the spatially averaged surface elemental and sometimes chemical composition.^{8–12} A number of these studies focused on the oxidation of duplex steels,^{8–10} where XPS could reveal the composition and oxidation states of the surface's oxides after various stages of controlled oxidation. The surface segregation during annealing of the 316L steel was studied using laboratory based XPS¹¹; however, in this study, the surface oxide was removed by sputtering prior to annealing. Although sputtered surface allows a clear interpretation of the XPS data, it makes it difficult to directly relate to the diffusion conditions in the presence of the native Cr surface oxides. With the advent of XPEEM, it has become possible to combine the spectroscopic information from photoemission with lateral imaging down to tens of nanometers.^{13–17}

A particular advantage of XPEEM is that the (potentially significant) variations in the chemical composition due to the grain structure of the metal and presence of inclusions become directly visible. Some XPEEM studies show the elemental and oxide distribution across the metal surfaces.^{13–16} A considerable focus in previous XPEEM work has been on oxidation under various controlled O₂ pressures.¹⁶ Additionally, a hard X-ray PEEM (HAXPEEM) study that extends the depth profiling on duplex steel using PEEM has been carried out.¹⁴ Finally, a PEEM study of the 316L steel,¹⁵ in which the sample was sputtered and annealed prior to imaging, revealed interesting information on the steel grains, but it did not provide information on the surface deoxidation.

In the present study, we focus on the deoxidation process, when the steel samples (with the native Cr-oxide present) are heated in vacuum. XPEEM provides information on the depth and lateral elemental as well as chemical state distribution at the surface, during the native oxide removal. Low-energy electron microscopy (LEEM) provides information on the morphology of the surface, visualizing individual grains. We prepare samples by specialized polishing to allow the sample to be imaged with high voltage in XPEEM and LEEM. No additional treatment is performed prior to measurements; thus, the samples have a native oxide close to the one found under manufacturing conditions. XPEEM allow XPS and X-ray absorption spectroscopy (XAS) of trace and alloying elements with extremely high surface sensitivity and nanoscale spatial resolution. As the sample can be heated in vacuum, we can follow the deoxidation with XPEEM/LEEM, observing how Mn and Si (which are present in small amounts in the bulk) diffuse to the surface and form oxides using the oxygen from the native Cr oxides. Vacuum annealing is relevant to industrial process as it is also used during vacuum brazing. In the present case, the vacuum pressure is lower than under industrial conditions. However, as it has previously been found that the qualitative behavior of oxide stability in the vacuum regime is similar across several orders of magnitude in pressure, while the precise transition temperature in the phase diagram might change.^{18,19} Although the vacuum level pressure of the present study is lower than in the industrial vacuum brazing process, it still provides qualitative information on the dynamic process as discussed below.

2 | MATERIALS AND METHODS

2.1 | Spectromicroscopy

Photoemission and low-energy electron microscopy experiments were performed at MAXPEEM, a dedicated beamline at MAX IV Laboratory. The beamline houses a state-of-the-art aberration-corrected spectroscopic photoemission and low-energy electron microscope (SPELEEM). This powerful instrument offers a wide range of complementary techniques providing structural, chemical, and magnetic sensitivity with a single-digit nanometer spatial resolution. This includes XPEEM and LEEM as well as XPS and XAS spectroscopy in selective areas down to a few tens of square nanometers. The beamline can

deliver a high photon flux in the range 30–1200 eV. In the MAXPEEM setup, the X-ray beam impinges on the sample at nominal incidence. The microscope is equipped with an aberration corrector which improves *both* the resolution *and* transmission. As a (photo)electron detector, a new CMOS TVIPS-F216 camera is used. In the present work, two different operation modes of the microscope have been used: *microscopy* and *spectroscopy* modes. In the *microscopy* mode, the image plane of the objective lens is displayed on the screen. The energy slit is placed at the dispersive plane of the energy analyzer, selecting only electrons with a given kinetic energy. The kinetic energy of the photoelectrons is set by applying a voltage bias, referred to as “start voltage,” to the sample. In the *spectroscopy* mode, the projector magnifies the dispersive plane at the end of the energy filter onto the screen. The intensity line profile over the spread (16 eV) electron beam reveals the energy distribution of the photoelectrons. Annealing was performed using electron bombardment filament placed behind the sample. Temperature was measured with a thermocouple placed just below the heater and an infrared pyrometer via a viewport. The base pressure in the measurement chamber is 1×10^{-10} mbar, during annealing the pressure raised to a maximum of 5×10^{-9} mbar. Low temperature ($\leq 550^\circ\text{C}$) annealing of the samples was carried out in the preparation chamber for 30 min. High-temperature ($> 550^\circ\text{C}$) annealing was carried out in the measurement chamber for a duration of 5 min in order to maintain the pressure in the low 10^{-9} mbar range. Subsequently, all spectra were recorded at room temperature.

2.2 | Sample preparation

Bulk metal was cut to cuboids sized 8 mm \times 8 mm \times 1 mm using a Struers Secotom 50 precision cutter and embedded in Struers Black MultiFast hot mounting resin (thermosetting bakelite with wood filler) at 180°C using Struers CitoPress-5 electro-hydraulic hot press. The samples were embedded with one face exposed on the bakelite surface. The exposed faces were polished using a Struers Tegramin-30 microprocessor controlled grinder set to pad rotation at 150 rpm and holder co-rotating at 150 rpm using the following recipe: (i) Struers Grey DiaDuo-2 9 μm (water-based suspension 9- μm diameter monocrystalline diamonds), (ii) Struers Blue DiaDuo-2 3 μm (water-based suspension 3- μm diameter monocrystalline diamonds), (iii) Struers White DiaDuo-2 1 μm (water-based suspension 1- μm diameter monocrystalline diamonds), and (iv) Struers DiaPro Nap $\frac{1}{4}$ μm (water-based diamond suspension). Steps (i)–(iii) were performed on Struers MD-Dac woven acetate pads, at 20 N pressure per sample, 2 min engagements with visual inspection and soap and water cleaning in-between. Step (iv) was performed on Struers MD-Nap short synthetic fiber polishing cloth, at 5 N pressure per sample and 4 min engagement. The samples were cleaned thoroughly in soapy water, rinsed in distilled water, and mechanically removed from the bakelite resin at room temperature. Samples were checked with atomic force microscopy (Figure S1) as described in supporting information.

3 | RESULTS AND DISCUSSION

3.1 | Initial visualization of the amorphous oxide removal and appearance of grains

To get an initial overview of surface topography of the 316L steel during annealing, we use LEEM in the so-called *Mirror* mode (Figure 1). In *Mirror* mode, the sample bias voltage is adjusted to allow minimal interaction of the electron beam with the surface. The contrast is determined by local variation in work function or height across the sample surface. Thus, any changes in morphology or local atomic scale structural termination (that leads to work function changes) of the surface will be visible.

In Figure 1, the surface of the 316L sample is imaged *live* upon annealing. Up to $\sim 620^\circ\text{C}$, the features in the images consist of a few lines and dark spots which we attribute to scratches and minor debris from the polishing (consistent with AFM images of steel samples after polishing, see Figure S1). As the process of oxide transformation/removal starts to occur, the underlying bulk grain structure becomes visible, as seen in Figure 1C,D. As this imaging mode is highly surface sensitive, we interpret this as an amorphous oxide being present initially, which is unaffected by the underlying grain structure and homogeneous on the resolution level of the LEEM images. As this oxide is reduced, the underlying grain structure, including boundaries, manifests in LEEM image due to diffraction contrast. The austenite FCC crystal grains exhibit different intensity depending on surface crystalline structure and orientations. In summary, the Cr oxide, which is covering the metal surface at low temperatures, is a continuous amorphous film lacking both grain boundaries and surface crystalline structure. After high temperature deoxidation, the grain boundaries of the underlying austenite Fe become visible. It can further be noted that up to 850°C , the grain morphology itself appears stable. To further elucidate the chemical changes of the surface oxide and the relation to the grains, we will turn to spectroscopic imaging in the next section.

3.2 | Elemental and chemical surface distribution as a function of annealing temperature

The surface chemistry was studied after annealing at several temperatures up to 850°C by chemical analysis of trace and alloying elements. Chemical analysis was performed in two different *spectroscopic* modes: direct photoemission (XPS) and X-ray absorption spectroscopy (XAS). In the XPS mode, the microscope is tuned to record intensity of an elemental core-level of interest. In the XAS mode, the photon energy is scanned over the elemental absorption edge while the change in secondary electron emission is recorded. The direct XPS mode is more surface sensitive typically probing 1–2 nm, while the absorption mode has a probing depth of 5–10 nm.²⁰

In Figure 2, we show the average spectroscopic signal across the surface of four elements as a function of annealing temperature. At room temperature, the main signal at the surface comes only from Cr

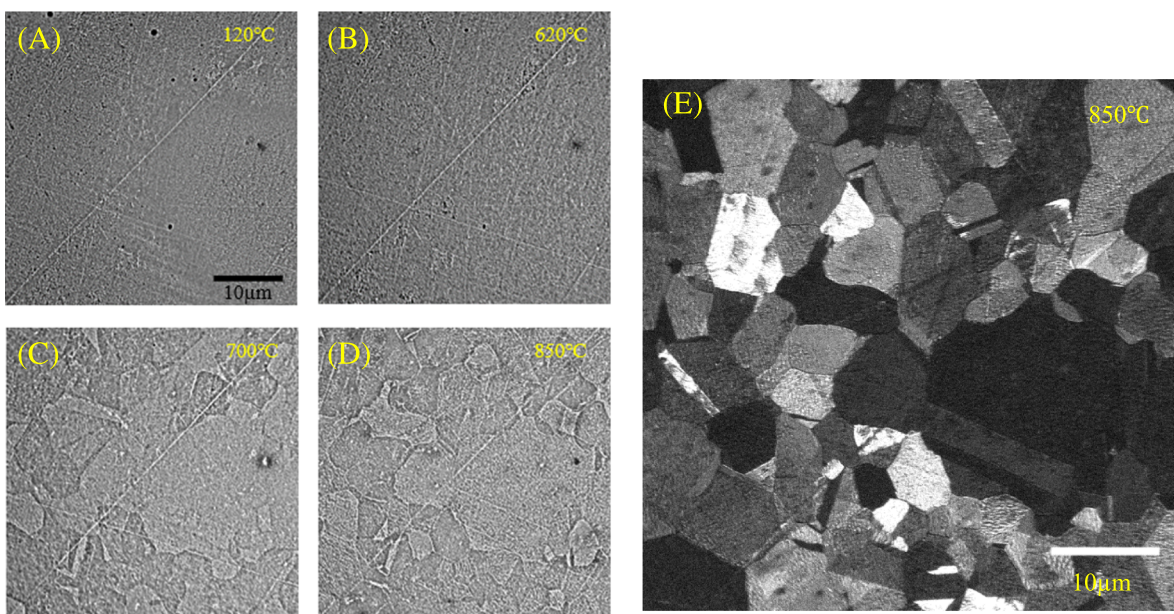


FIGURE 1 (A–D) MEM images of the same surface annealed at different temperatures (120°C, 620°C, 700°C, and 850°C, respectively). The annealing temperature is shown at the upright corner of image. The grain boundaries start to be seen in (C), indicating that it occurred between 620°C and 700°C. LEEM (electron kinetic energy: 3.15 eV) image obtained after annealing at 850°C. The contrast coming from the crystal structure of the grains at the surface, which is different due to their different orientations. Images on (A–D) are of identical size, the scale bars as seen in (A) and (E) are 10 μm

in the form of metallic Cr and Cr oxide (a double peak at 577 eV in the Cr L-edge XAS spectrum), as shown in Figure 2C. For reference, we briefly mention overview XPS measurements done in previous studies of the mechanically polished 316L alloy prior to heat treatments.^{12,22,23} Compared with the bulk ratios for this alloy, the Cr/Fe ratio is ~3 times larger at the surface compared with the bulk composition, while the relative amount of Ni is similar to the bulk values. Other elements that exist in small amounts inside the alloy can also be detected in small amounts at the surface. Returning to the present study, we find that upon annealing, the Cr oxide component markedly decreases and disappears above 850°C. The oxide evolution can also be traced by recording the direct photoemission signal from O. Figure 2A shows XPS measurements of O1s peak as a function of temperature. Upon annealing, the O1s peak area is steady up to 570°C, at which point it decreases with ~50% from 570°C to 700°C and then the peak disappears at 850°C (indicating complete surface oxide removal). The peak position shifts towards higher binding energy as the temperature increase. In particular, the significant change at 700°C coincides with the appearance of a strong Si2p peak appearing (see Figure 2B). A steady shift of the O1s peak towards higher binding energies together with a similar shift of the Si2p peak is an indication of Si oxide formation at elevated temperatures. The Si2p XPS data are consistent with formation of four different suboxides Si₂O, SiO, Si₂O₃, and SiO₂, which have binding energy 100.6, 101.7, 102.5, and 103.4 eV, respectively.²⁴ The binding energy of Si2p at 700°C (103.5 eV, Figure 2B) indicates that SiO₂ forms at the surface while a doublet at low binding energy side at 100 eV (700°C, the orange curve) is elemental silicon.²⁴ Both O1s

and Si2p peaks disappear above 850°C, when SiO_x starts to leave the surface. At around 550°C, a strong increase in the Mn signal is detected (Figure 2D) in the form of an oxide, as can be deduced by comparing with a MnO XAS reference spectrum²¹ (shown in Figure 2D). Both Si or Mn are only present in small amounts at the surface in the spectra recorded at room temperature and 120°C, which is consistent with the low amounts in bulk samples. The Mn appears in large amounts at lower annealing temperatures than the Si, but also starts to be removed earlier from the surface. The large increase in Mn and Si content at higher temperatures indicates that the two elements diffuse from the bulk to the surface area in substantial amounts. The observation that Si and Mn appear as oxides at the same temperature where Cr-oxide starts to decompose indicate that the metallic Si and Mn absorbs the oxygen atoms from the decomposing metal oxides Cr-oxide as well as Fe-oxides (O levels in 316L steel is only a few tens of ppm). The observations can be interpreted as O moving from the Cr-oxides to form Si and Mn oxides, while some O also evaporates into the vacuum. Finally, it can be seen that both the Si and Mn peaks disappear when the annealing temperature reaches 850°C. This show that these metal oxides either evaporate into the vacuum or the elements diffuse back into the bulk upon removal of the O. Both Si and Mn spectra indicate that they sustain their oxide nature until they evaporate; no trace of elemental species is observed. It is known that SiO₂ evaporate at the temperatures upon which Si is observed to disappear, consistent with the direct evaporation of the Si-oxide.²⁵ Mn has a high vapor pressure at these temperatures, which would be in favor of the element evaporating.^{11,26,27}

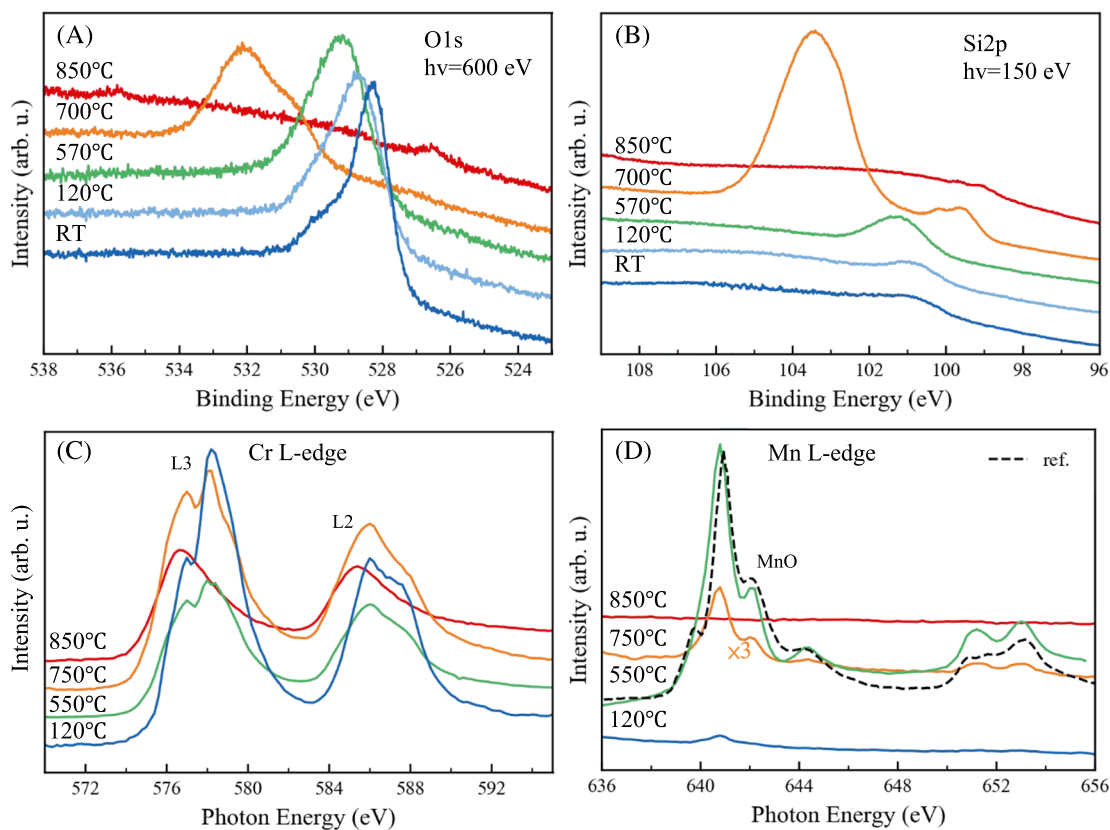


FIGURE 2 Core-level X-ray photoemission spectra (XPS) for O1s (A) and Si2p (B) acquired after annealing at different temperatures. X-ray absorption spectra (XAS) for Cr L-edge (C) and Mn L-edge (D). Cr L-edge spectra (C) upon annealing display a smooth transition from Cr oxide (the blue curve, 120°C) to a metallic Cr (the red curve, 850°C). Mn L-edge XAS show manganese segregation at the surface in the form of manganese oxide. The signal drops markedly, and no traces of manganese can be detected at 850°C. In the MnO XAS plot, a reference spectrum for Mn oxide (black dash line) is presented with a small (0.6 eV) energy shift²¹

Previous XPS measurements on stainless steels also found surface out-diffusion of Mn and Si during heating.¹¹ In that study, sputtering was conducted prior to annealing resulting in a very different initial surface composition. This could indicate that the elemental out-diffusion of Mn and Si is a general phenomenon independent of initial surface conditions. Further, no oxygen was initially present,¹¹ but some O emerged at the surface at later stages of the annealing. Thus, the native oxides could also play a role in stabilizing the metal impurities at the surface. A significant increase in Cr content found in Gröning et al.¹¹ is not observed in the present study, presumably due to their initial removal of the Cr-oxide at the surface. The different results indicate that a preferred elemental and chemical balance is likely to exist at the surface related to energetics.

Cr-oxide decomposition can be followed in more detail by two-component fitting of the Cr L-edge absorption spectra (Figure 3). The spectra at lowest (120°C) and highest (850°C) temperatures were used as reference for oxide and metallic Cr, assuming that Cr is 100% oxidized and metallic, respectively. The examples of spectra were fitted (linear regression) with two components (i.e., oxide and metal) at 550°C (Figure 3A) and 700°C (Figure 3B). The fit coefficients are shown in the legend. The areas of oxide (blue shade) and metallic Cr (red shade) were used to calculate the percentage of oxide and

metallic Cr at different temperatures as shown in Figure 3C. It can be seen that the oxide removal, which reaches about 50% at 700°C, coincides with the formation of Mn and Si oxides. Thus, a combination of both O binding to the Si and Mn instead of Cr, as well as O evaporating into the vacuum, can explain this observation. At 850°C, O is gone, and only metal Cr is left, which is consistent with no peak being observed in the O1s spectra. Finally, Ni and Fe spectroscopic imaging was also performed, and average spectra deduced as seen in Figure 4. The shape of the Fe L-edge after annealing at 120°C (Figure 4, left, blue solid curve) can be associated with the presence of oxidized Fe,²⁸ while the spectra observed after annealing to 750°C (Figure 4, left, orange dash curve) is more similar to metallic Fe.²⁸ The missing O can be either taken up by the Mn and Si (as discussed above) or evaporate into the vacuum. The amount of Ni at the surface appears to decrease as the sample is annealed, and no significant chemical change is observed for the Ni. Here, it can be noted that previous ab initio calculations of alloy compounds have found that while Ni segregation in metallic alloys can be favorable at room temperature, this trend starts to reverse at higher temperatures.²⁹ Another similar study³⁰ has found that the presence of O strongly influences the segregation of Cr at room temperature, leading to the segregation and high abundance of Cr.

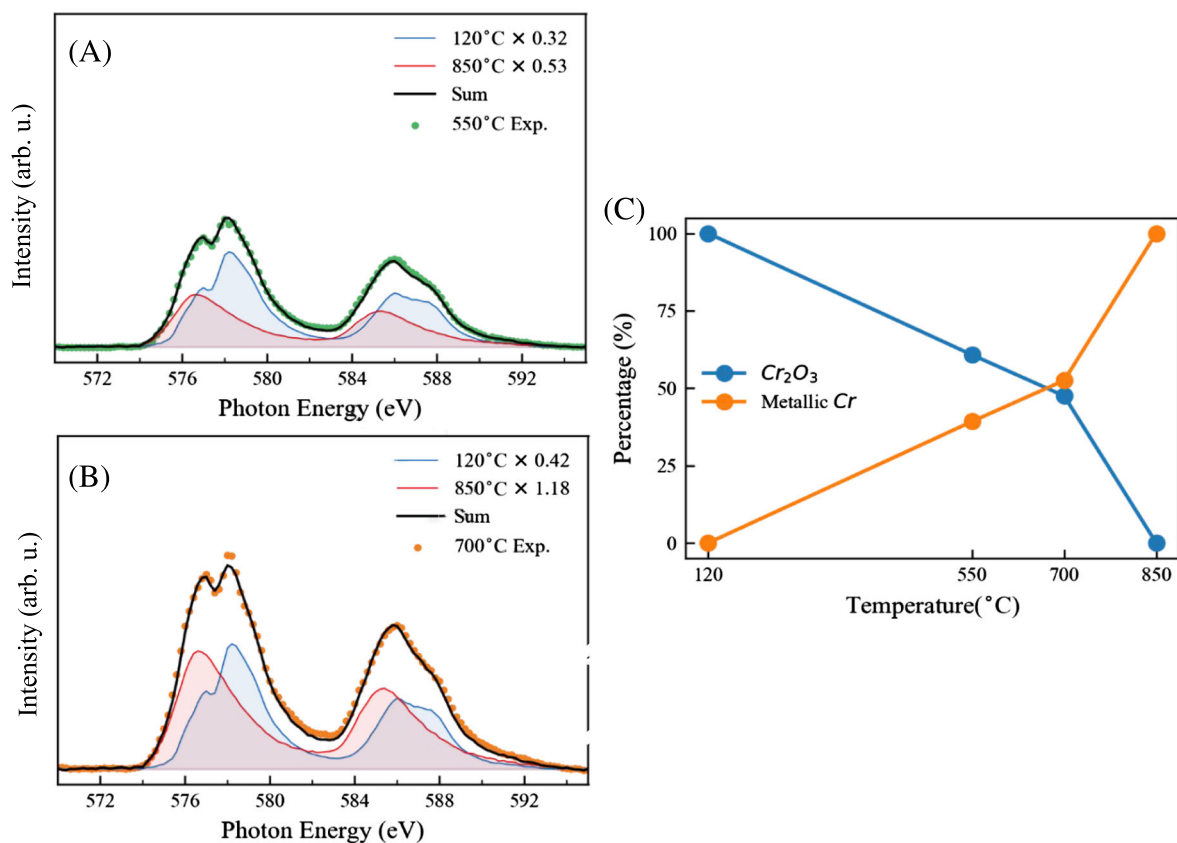


FIGURE 3 XAS spectra fitting of Cr based on the XAS spectrum for Cr L-edge with background removed at different temperatures as seen in Figure 2C. The spectra at lowest (120°C) and highest (850°C) temperatures are taken as references for oxide and metallic Cr, respectively. The spectra fitting (linear regression) with two components (the oxide and metal ones) are shown for 550°C (A) and 700°C (B). The fitting coefficients are shown in the legend. (C) The areas of Cr_2O_3 (blue shade) and metallic Cr (red shade) were used to calculate the percentage of Cr_2O_3 and metallic Cr at different temperatures

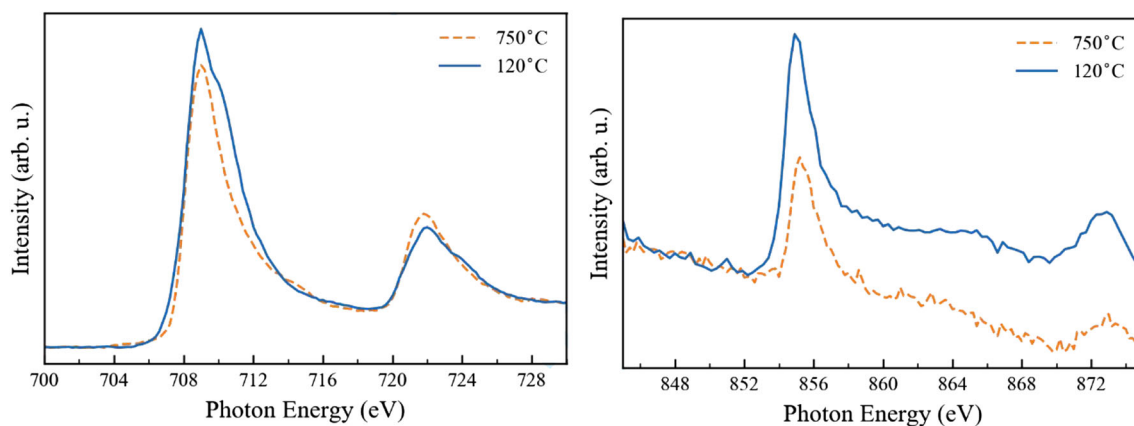


FIGURE 4 XAS for Fe L-edge (left) and Ni L-edge (right) from sample AISI 316L after annealing at 120°C and 750°C. (left) The Fe L-edge exhibits sharp 2p_{3/2} and 2p_{1/2} peaks where shoulders at higher photon energies can be seen after annealing at 120°C. These extra peaks can be associated with the presence of an iron oxide²⁸

3.3 | Lateral distribution of elements and their chemical states at surface

An important question that can be answered using XPEEM is the distribution of elements and chemical species laterally across the surface.

Prior to the grains becoming visible at 650°C–700°C, the featureless appearance of the MEM and XPEEM images indicates that the chemical components are homogeneously distributed across the surface (except differences due to the polishing scratches) on the length scales visible in the PEEM images (20 μm –10 nm). Figure 5A shows a

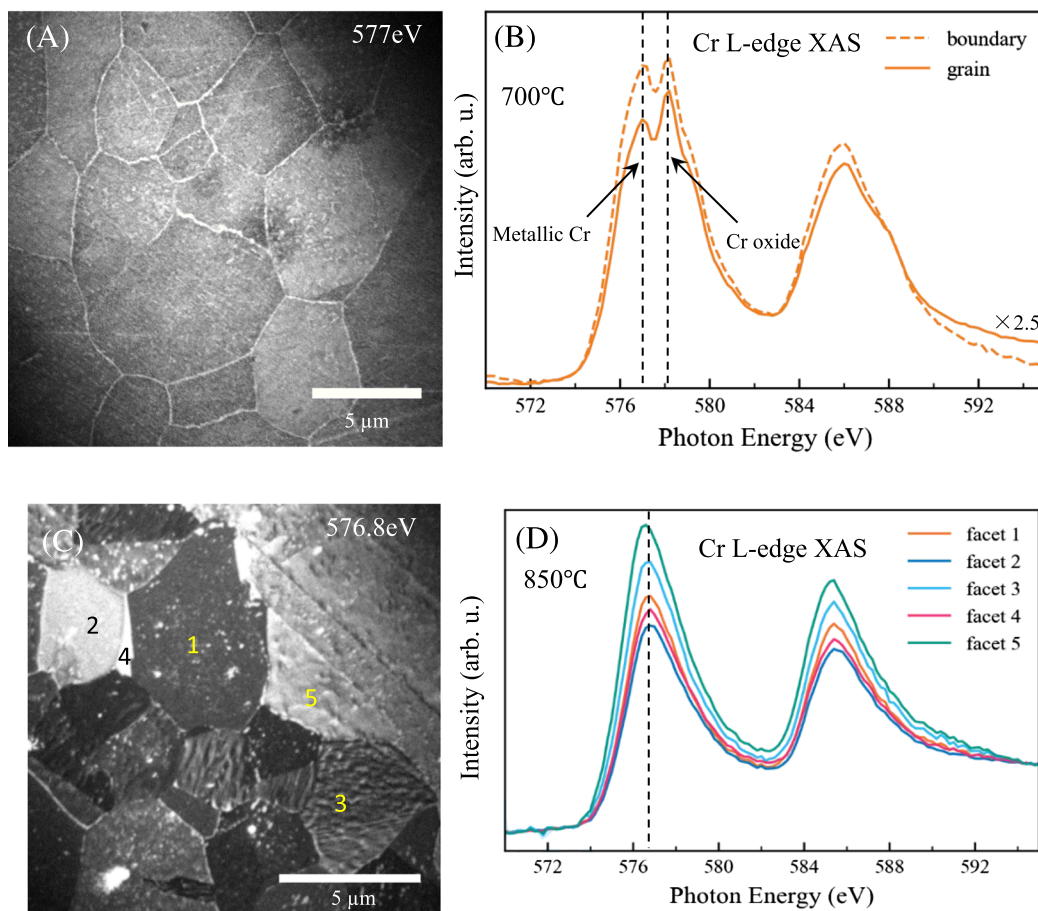


FIGURE 5 Chemical mapping of the grain boundaries. (A) XPEEM image at photon energy 577 eV after annealing at 700°C. (B) Cr L-edge XAS from grain boundaries and grains regions. Metallic component of Cr (at 577 eV photon energy) is significantly higher at the grain boundaries compared with the oxide one (at 578 eV photon energy). (C) XPEEM image acquired at the edge (photon energy 576.8 eV) of the Cr absorption spectra after annealing at 850°C. (D) XAS spectra from five different grains labelled in (C). The intensities of the absorption spectra show the different Cr content in different grains. All XAS spectra are normalized by pre-edge values at the same position in the image to remove background effects

secondary electron image recorded using electrons with a photon energy of 577 eV (the Cr oxide maximum in the XAS spectra) after annealing to 700°C. The grain boundaries can be clearly seen. However, to robustly analyze the difference between the grain boundary and grain, we extract spectra from a grain center and a grain boundary, respectively. The results are shown in Figure 5B where the intensity is plotted as a function of photon energy. The areas used to generate the spectra were of the same size and close to each other, so that they can be properly compared. These results show that after annealing at high temperatures, a larger content of metallic Cr is present along grain boundaries. Further insights can be gained from measuring XAS spectra of Cr from several grains after annealing to 850°C (after complete removal of O), as seen in Figure 5C,D. It can be seen that the Cr content in the surface region of the grains varies significantly from grain to grain. A below threshold image (Figure 5C) also shows a grain boundary contrast, which is consistent with the fact that the work function (WF) of the metallic Cr (4.5 eV) is lower than

the WF of Iron (4.7–4.8 eV).²⁷ So after annealing at high temperatures, we observe segregation of metallic Cr along grain boundaries.

For Si and Mn, a more qualitative analysis was done in the temperature range between 500°C and 700°C when they are abundant on the surface. This is done by comparing images recorded at the core-level peak/adsorption edge of the materials versus off the peak as shown in Figures S3 and S4. At 550°C, before the grain boundaries become visible, both Mn and Si appear evenly distributed within the resolution limits of the PEEM. After annealing to 750°C, when the grains become visible, we find that Mn and Si are present in significant quantities both on the grains and on the grain boundaries. For Si, a difference in abundance between grain interior and grain boundary is not observable, while Mn is slightly more abundant on the grain boundaries. It has previously been suggested that Mn and Si diffuse along the grain boundaries to the surface.¹¹ While this cannot be excluded, the present study is not consistent with Mn and Si remaining at the grain boundaries. If Mn and Si do diffuse along the

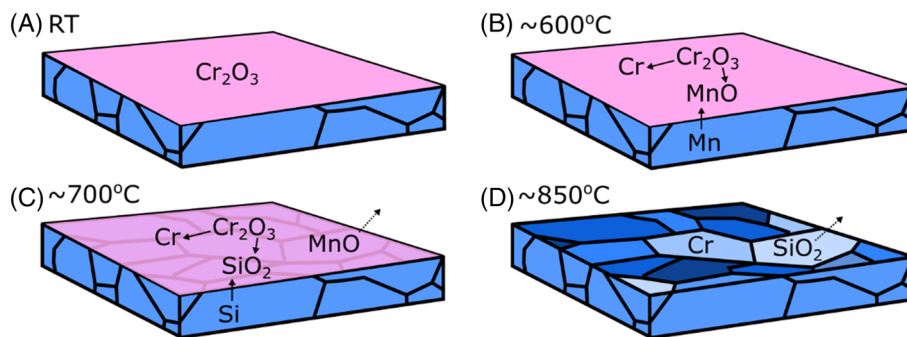


FIGURE 6 Schematic representation of a deoxidation model which is compatible with the findings: (A) at room temperature the surface is covered by an amorphous and homogeneous Cr based oxide, with trace amounts of bulk elements. (B) At approximately 600°C, the Cr oxide signal weakens, and metallic Cr and MnO appear due to Mn diffusion from the bulk. (C) At approximately 700°C, the Cr oxide signal continues to weaken, metallic Cr signal grows, MnO signal weakens as it evaporates, and SiO₂ signal appears due to Si diffusion from the bulk and O capture from the Cr oxides. (D) At approximately 850°C, SiO₂ signal disappears, and the metallic Cr signal indicates slightly different Cr content on different grains and at boundaries

grain boundaries, at least these elements rapidly spread out laterally when reaching the surface.

3.4 | A qualitative model of the deoxidation

We now summarize the findings in a qualitative model of the deoxidation process by in-vacuum annealing, as seen in Figure 6. Initially, the surface consists of Cr oxide with small amounts of other elements such Si, Mn, and Ni. As the temperature is increased (to ~500°C), Mn diffuses to the surface of the sample and oxidizes binding to O released from the reducing Cr-oxides. As the annealing temperature is further increased to ~700°C, the Mn is removed completely from the surface region likely due to evaporation. The amorphous Cr₂O₃ layer start to lose O and break up during this annealing. The Cr still remains at the surface but gradually becomes metallic as the O is removed. Silicon starts to diffuse onto the surface and oxidize with a strong increase of Si observed after annealing to 700°C. SiO₂ and O evaporate from the surface at 850°C. Thus, after annealing to 850°C, the Si, O, and Mn have been removed from the surface, leaving only Cr and Ni on the surface. Recent ab initio calculations addressing the energetics of surface segregation in Cr-Mn-Fe-Co-Ni alloys^{29,30} give further important insights into the surface deoxidation process, showing that, in presence of O, it is energetically favorable for Cr and Mn to segregate towards the surface. These findings, obtained for a wide range of compositions, are consistent with our results. Further we note the surface segregation of other trace elements has been studied theoretically for pure metal alloys in vacuum²⁹ showing qualitative changes as the temperature increase with an increase in the alloy elements at the surface at the expense of Ni. Consistent with these studies, we do see a decrease in Ni surface content at increasing temperature and in particular an increase for Mn.

We can also use energetics from first principle calculations to understand the transfer of O, first from Cr to Mn and later from Mn

to Si, that occur in parallel to the Mn and Si migration to the surface. The formation free energies of MnO₂ and Cr₂O₃ are both much higher than Fe₂O₃ at room temperature, as derived from³⁰ (Cr₂O₃ being slightly more favorable). The formation energies are influenced by an increase in temperature,^{31,32} and the energy balance between some of the oxides will depend on precise compositions. Thus, the removal of the O from the original metal oxides at the surface by the Mn at high temperatures could be explained by the formation energies, although some more calculations in relation to the balance between Cr and Mn oxides for this particular case would be interesting to complete the picture. The surface energetics of Si and SiO₂ for the steel systems are not available, but both calculations and experimental verification of formation energies of bulk oxide compounds³³ show that SiO₂ is highly energetically favorable compared with Cr, Fe, and Mn oxides. In conclusion, the presented model and observed data are consistent with available theoretical calculations although for the complete understanding of the Mn and Si segregation as well as preferential oxidation further calculations would be relevant. Ab initio calculations appear to form a good basis for understanding these systems, but it would be interesting to investigate when for example kinetic effects will start to play a role, as has been seen in the oxide formation in single element alloys.¹⁹

While the crystalline Fe grains can be observed at the surface as the Cr oxide begin to decompose, this initial protective oxide and the initial distribution of trace elements is amorphous and homogeneous in distribution in the tens of microns to tens of nanometers range.

Already, during annealing, there is a tendency of the Cr to gather in the grain boundaries of the Fe, with these boundaries being particularly rich in metallic Cr. After annealing, there is a nonhomogeneous Cr distribution at the surface among different grains and with some Cr segregation along the grain boundaries. In contrast, Si and Mn appear homogeneously distributed over the surface before they are removed at high temperatures.

4 | PERSPECTIVES

Elucidating the stainless-steel surface decomposition and role of alloying and trace elements can potentially be used to optimize the vacuum furnace programs, generating shorter lead times and more efficient manufacturing. However, while oxidation has been studied more extensively, the important initial step of deoxidation has been much less studied. In particular, it is important to begin with the initial native oxide that is also the starting point when processing the steel. The study indicates that the deoxidation can potentially be significantly altered with tailored addition of small amounts of elements of both the stainless steel. Future studies of different steel compounds in the context of the deoxidation would be interesting to further investigate the influence of trace compounds, as they will affect each other as they rapidly diffuse across and into the surface while exchanging for example O.

ACKNOWLEDGEMENTS

This work was supported by the Swedish Research Council (VR), the Swedish Foundation for Strategic Research (SSF), and Vinnova.

ORCID

Lin Zhu  <https://orcid.org/0000-0002-6503-3386>

Filip Lenrick  <https://orcid.org/0000-0001-6969-1215>

Anders Mikkelsen  <https://orcid.org/0000-0002-9761-0440>

REFERENCES

- Adams RO. A review of the stainless steel surface. *J Vac Sci Tech A*. 1983;1(1):12-18. <https://doi.org/10.1116/1.572301>
- Olsson C-OA, Landolt D. Passive films on stainless steels—chemistry, structure and growth. *Electrochimica Acta*. 2003;48(9):1093-1104. [https://doi.org/10.1016/s0013-4686\(02\)00841-1](https://doi.org/10.1016/s0013-4686(02)00841-1)
- Value added and jobs resulting from joining technology in Germany and in Europe. https://www.die-verbundungs-spezialisten.de/fileadmin/user_upload/Broschueren/Wertschoepfungsstudie/Summary_Value_Added_Study_15_Pages.pdf, 2013 (accessed 21 February 2021).
- Way M, Willingham J, Goodall R. Brazing filler metals. *Int Mater Rev*. 2020;65(5):257-285. <https://doi.org/10.1080/09506608.2019.1613311>
- Ellingham HJT. Reducibility of oxides and sulphides in metallurgical processes. *J Soc Chem Ind*. 1944;63(5):125-160. <https://doi.org/10.1002/jctb.5000630501>
- Schwartz MM. *Brazing*. 2nd ed. ASM international; 2003.
- Eustathopoulos N, Hodaj F, Kozlova O. The wetting process in brazing. In: Sekulić DP, ed. *Advances in Brazing*. Woodhead Publishing; 2013:3-30.
- Donik Č, Kocijan A, Grant JT, Jenko M, Drenik A, Pihlar B. XPS study of duplex stainless steel oxidized by oxygen atoms. *Corros Sci*. 2009; 51(4):827-832. <https://doi.org/10.1016/j.corsci.2009.01.021>
- Donik Č, Mandrino D, Jenko M. Depth profiling and angular dependent XPS analysis of ultra thin oxide film on duplex stainless steel. *Vacuum*. 2010;84(11):1266-1269. <https://doi.org/10.1016/j.vacuum.2010.01.057>
- Mandrino Dj, Donik Č. Chemical-state information obtained by AES and XPS from thin oxide layers on duplex stainless steel surfaces. *Vacuum*. 2011;86(1):18-22. <https://doi.org/10.1016/j.vacuum.2011.03.025>
- Gröning P, Nowak S, Schlapbach L. Temperature-dependent surface modifications of AISI 316L and AISI 440C stainless steel substrates. *Appl Surf Sci*. 1991;52(4):333-337. [https://doi.org/10.1016/0169-4332\(91\)90076-v](https://doi.org/10.1016/0169-4332(91)90076-v)
- Mandrino D, Godec M, Torkar M, Jenko M. Study of oxide protective layers on stainless steel by AES, EDS and XPS. *Surf Interface Anal*. 2008;40(3-4):285-289. <https://doi.org/10.1002/sia.2718>
- Roesse P, Keutner C, Berges U, Espeter P, Westphal C. Photoemission Electron Microscopy as a Tool for Studying Steel Grains. *Metall Mater Trans A*. 2017;48(3):1484-1490. <https://doi.org/10.1007/s11661-016-3911-y>
- Långberg M, Örnek C, Zhang F, et al. Characterization of Native Oxide and Passive Film on Austenite/Ferrite Phases of Duplex Stainless Steel Using Synchrotron HAXPEEM. *J Electrochem Soc*. 2019;166(11):C3336-C3340. <https://doi.org/10.1149/2.0421911jes>
- Barrett N, Renault O, Lemaître H, et al. Microscopic work function anisotropy and surface chemistry of 316L stainless steel using photoelectron emission microscopy. *J Electron Spectrosc Relat Phenom*. 2014;195:117-124. <https://doi.org/10.1016/j.elspec.2014.05.015>
- Kang T-H, Ihm K, Hwang C-C, et al. Direct image observation of the initial forming of passive thin film on stainless steel surface by PEEM. *Appl Surf Sci*. 2003;212-213:630-635. [https://doi.org/10.1016/s0169-4332\(03\)00137-5](https://doi.org/10.1016/s0169-4332(03)00137-5)
- Ali-Löytty H, Hannula M, Juuti T, Niu Y, Zakharov AA, Valden M. The role of (FeCrSi)₂(MoNb)-type Laves phase on the formation of Mn-rich protective oxide scale on ferritic stainless steel. *Corros Sci*. 2018; 132:214-222. <https://doi.org/10.1016/j.corsci.2017.12.026>
- Weiss W, Ranke W. Surface chemistry and catalysis on well-defined epitaxial iron-oxide layers. *Progr Surf Sci*. 2002;70(1-3):1-151. [https://doi.org/10.1016/s0079-6816\(01\)00056-9](https://doi.org/10.1016/s0079-6816(01)00056-9)
- Lundgren E, Gustafson J, Mikkelsen A, et al. Kinetic Hindrance during the Initial Oxidation of Pd(100) at Ambient Pressures. *Phys Rev Lett*. 2004;92(4):046101-1-046101-4. <https://doi.org/10.1103/physrevlett.92.046101>
- Frazer BH, Gilbert B, Sonderegger BR, De Stasio G. The probing depth of total electron yield in the sub-keV range: TEY-XAS and X-PEEM. *Surf Sci*. 2003;537(1-3):161-167. [https://doi.org/10.1016/s0039-6028\(03\)00613-7](https://doi.org/10.1016/s0039-6028(03)00613-7)
- Gilbert B, Frazer BH, Belz A, et al. Multiple Scattering Calculations of Bonding and X-ray Absorption Spectroscopy of Manganese Oxides. *Chem A Eur J*. 2003;107(16):2839-2847. <https://doi.org/10.1021/jp021493s>
- Hryniewicz T, Rokosz K, Rokicki R. Electrochemical and XPS studies of AISI 316L stainless steel after electropolishing in a magnetic field. *Corros Sci*. 2008;50(9):2676-2681. <https://doi.org/10.1016/j.corsci.2008.06.048>
- Hryniewicz T, Rokosz K. Analysis of XPS results of AISI 316L SS electropolished and magnetoelectropolished at varying conditions. *Surf Coat Technol*. 2010;204(16-17):2583-2592. <https://doi.org/10.1016/j.surfcoat.2010.02.005>
- Bashouti MY, Sardashti K, Ristein J, Christiansen SH. Early stages of oxide growth in H-terminated silicon nanowires: determination of kinetic behavior and activation energy. *Phys Chem Chem Phys*. 2012; 14(34):11877. <https://doi.org/10.1039/c2cp41709j>
- Frantsuzov AA, Makrushin II. Growth of an oxide film on a clean silicon surface and the kinetics of its evaporation. *Thin Solid Films*. 1976; 32(2):247-249. [https://doi.org/10.1016/0040-6090\(76\)90305-9](https://doi.org/10.1016/0040-6090(76)90305-9)
- Wellbeloved DB, Craven PM, Waudby JW. Manganese and manganese alloys. In: *Ullmann's Encyclopedia of Industrial Chemistry*; 2000: 175-221. https://doi.org/10.1002/14356007.a16_077
- Lide DR. *CRC Handbook of Chemistry and Physics*. Boca Raton, Fla.; London: CRC Press Taylor & Francis [distributor]; 2008:12-114.
- López MF, Gutiérrez A, Torres CL, Bastidas JM. Soft x-ray absorption spectroscopy study of electrochemically formed passive layers on

- AISI 304 and 316L stainless steels. *J Mater Res.* 1999;14(3):763-770. <https://doi.org/10.1557/jmr.1999.0102>
29. Ruban AV. On segregation in multicomponent alloys: Surface segregation in austenite and FeCrCoNiMn alloys. *Comput Mater Sci.* 2021;187:110080-110084. <https://doi.org/10.1016/j.commatsci.2020.110080>
30. Ferrari A, Körmann F. Surface segregation in Cr-Mn-Fe-Co-Ni high entropy alloys. *Appl Surf Sci.* 2020;533:147471-147477. <https://doi.org/10.1016/j.apsusc.2020.147471>
31. Mutter D, Urban DF, Elsässer C. Determination of Formation Energies and Phase Diagrams of Transition Metal Oxides with DFT+U. *Materials.* 2020;13(19):4303-4324. <https://doi.org/10.3390/ma13194303>
32. Anzini E, Glaenger N, Mignanelli PM, Hardy MC, Stone HJ, Pedrazzini S. The effect of manganese and silicon additions on the corrosion resistance of a polycrystalline nickel-based superalloy. *Corros Sci.* 2020;176:109042-109052. <https://doi.org/10.1016/j.corsci.2020.109042>
33. Hautier G, Ong SP, Jain A, Moore CJ, Ceder G. Accuracy of density functional theory in predicting formation energies of ternary

oxides from binary oxides and its implication on phase stability. *Phys Rev B.* 2012;85(15):155208-1-155208-18. <https://doi.org/10.1103/physrevb.85.155208>

SUPPORTING INFORMATION

Additional supporting information may be found in the online version of the article at the publisher's website.

How to cite this article: Zhu L, Al-Sakeeri A, Lenrick F, et al. Surface chemistry and diffusion of trace and alloying elements during in vacuum thermal deoxidation of stainless steel. *Surf Interface Anal.* 2021;1-10. doi:10.1002/sia.7024